The homozygous variant c.797G>A/p.(Cys266Tyr) in PISD is associated with a Spondyloepimetaphyseal dysplasia with large epiphyses and disturbed mitochondrial function

The Homozygous Variant c.797G>A/p.(Cys266Tyr) in *PISD* is Associated with a Spondyloepimetaphyseal Dysplasia with Large Epiphyses and Disturbed Mitochondrial Function

Katta M. Girisha[1#],* Leonie von Elsner[2#], Kausthubham Neethukrishna[1], Mamta Muranjan[3,4], Anju Shukla[1], Gandham SriLakshmi Bhavani[1], Gen Nishimura[5], Kerstin Kutsche[2#],* and Geert Mortier[6#]

[1]Department of Medical Genetics, Kasturba Medical College, Manipal Academy of Higher Education, Manipal, 576104, India

[2]Institute of Human Genetics, University Medical Center Hamburg-Eppendorf, 20246 Hamburg, Germany

[3]Department of Clinical Genetics, Seth GS Medical College and KEM Hospital, Mumbai, 400012, India

[4]Consultant in Clinical Genetics, P.D. Hinduja National Hospital & MRC, Mumbai 400012, India.

[5]Department of Pediatric Imaging, Tokyo Metropolitan Children's Medical Center, Fuchu, 183-8561, Japan

[6]Centre of Medical Genetics, University of Antwerp & University Hospital Antwerp, 2610 Antwerp, Belgium

[#] equally contributing

***Correspondence to:** girish.katta@manipal.edu and kkutsche@uke.de

This article has been accepted for publication and undergone full peer review but has not been through the copyediting, typesetting, pagination and proofreading process, which may lead to differences between this version and the Version of Record. Please cite this article as doi: 10.1002/humu.23693.

Word count: 166 characters (title), 197 words (abstract), 30 pages (main text), 5 (figures total), 2 (color figures)

Grant sponsor: The Department of Science and Technology, Government of India (project titled 'Application of autozygosity mapping and exome sequencing to identify genetic basis of disorders of skeletal development'; SB/SO/HS/005/2014) to Katta M. Girisha and the Deutsche Forschungsgemeinschaft (KU 1240/6-2) to Kerstin Kutsche.

Abstract

Spondyloepimetaphyseal dysplasias (SEMD) are a group of genetically heterogeneous skeletal disorders characterized by abnormal vertebral bodies and epimetaphyseal abnormalities. We investigated two families with a new SEMD type with one proband each. They showed mild facial dysmorphism, flat vertebral bodies (platyspondyly), large epiphyses, metaphyseal dysplasia, and hallux valgus as common clinical features. By trio-exome sequencing, the homozygous missense variant c.797G>A p.(Cys266Tyr) in *PISD* was found in both affected individuals. Based on exome data analyses for homozygous regions, the two patients shared a single homozygous block on chromosome 22 including *PISD*, indicating their remote consanguinity. *PISD* encodes phosphatidylserine decarboxylase that is localized in the inner mitochondrial membrane and catalyzes the decarboxylation of phosphatidylserine to phosphatidylethanolamine (PE) in mammalian cells. PE occurs at high abundance in mitochondrial membranes. Patient-derived fibroblasts showed fragmented mitochondrial morphology. Treatment of patient cells with MG-132 or staurosporine to induce activation of the intrinsic apoptosis pathway revealed significantly decreased cell viability with increased caspase-3 and -7 activation. Remarkably, ethanolamine supplementation largely restored cell viability and enhanced apoptosis in MG-132-stressed patient

cells. Our data demonstrate that the bi-allelic hypomorphic *PISD* variant p.(Cys266Tyr) is associated with a novel SEMD form, which may be treatable with ethanolamine administration.

Key words: spondyloepimetaphyseal dysplasia, phosphatidylserine decarboxylase, phosphatidylethanolamine, mitochondrial dysfunction, hypomorphic mutation

Introduction

Spondyloepimetaphyseal dysplasias (SEMD) are a group of genetically heterogenous skeletal dysplasias, radiographically characterized by abnormal (usually flattened) vertebral bodies and epimetaphyseal irregularities and often associated with disproportionate short stature. The differential diagnosis of subtypes of SEMDs is not an easy task because of overlapping pattern and severity of skeletal changes among the SEMD entities (Bonafe et al., 2015). The diagnosis can be facilitated by the observation of unique clinical and/or radiographic signs, but often it requires a genomic testing approach by either whole exome sequencing or a targeted skeletal dysplasia gene panel testing. The pathogenesis of SEMDs is heterogeneous. Recently, a group of skeletal dysplasias due to abnormalities of mitochondrial proteins have attracted attention (Guernsey et al., 2009; Ng et al., 2010; Pansuriya et al., 2011; Smith et al., 2014; Strauss et al., 2015). Here we describe two children with a newly recognized spondyloepimetaphyseal dysplasia with large epiphyses due to a homozygous missense mutation in *PISD*, which encodes the mitochondrial phosphatidylserine decarboxylase that catalyzes decarboxylation of phosphatidylserine to phosphatidylethanolamine.

Material and Methods

Family ascertainment

We identified two Indian families with one affected child each and obtained informed written consents from all participants in this study. This research was prospectively reviewed and approved by a duly constituted ethics committee.

Whole exome sequencing (WES) and variant filtering

Genomic DNA was extracted from whole blood of probands and parents using phenol-chloroform method. Genomic capture was carried out with Illumina's Nextera Rapid Capture Exome Kit followed by massively parallel sequencing on an Illumina NextSeq Platform (Illumina, San Diego, California, USA). The average coverage depth was 130x, with ~95% of the bases covered at >20x, and a sensitivity of >90%. WES data was analyzed using the in-house pipeline based on BWA (v0.7.15) (Li & Durbin, 2009) and GATK best practices (v3.6) (McKenna et al., 2010). The variant call format (vcf) files were annotated using ANNOVAR (K. Wang, Li, & Hakonarson, 2010; Yang & Wang, 2015) and then integrated with OMIM phenotypes, HPO terms and allele frequency details from in-house variant database of 475 exomes of Indian origin.

Variants with minor allele frequency <2% were filtered against population databases such as Exome Aggregation Consortium (ExAC), gnomAD and in-house variant database. Exonic and splice variants were then prioritized by pathogenicity assessment using multiple *in-silico* tools (SIFT, PolyPhen2, LRT, MutationTaster, Provean and M-CAP). Additionally, the genotype quality, read

frequencies and read depth of variants were also assessed. Detailed variant filtering strategy is outlined in Supp. Table S1.

Regions of homozygosity (ROH) and haplotype analysis

Homozygosity mapping was performed using the HOMWES tool (Kancheva et al., 2016). The vcf files of both probands were given as input and GenomeComb package default parameters were used to identify the ROH. The common ROH region obtained from homozygosity mapping analysis was then manually checked in exome sequencing data to identify the shared haplotype.

Conservation analysis

To assess the evolutionary conservation of the pathogenic sequence variant observed in *PISD* multiple sequence alignment was performed using Clustal Omega. For this analysis the *PISD* orthologs of the following species were considered from NCBI database: *Homo sapiens, Pongo abelii, Macaca nemestrina, Papio anubis, Canis lupus familiaris, Mus musculus, Octodon degus* and *Danio rerio*. Additionally, amino acid conservation was also evaluated using the ConSurf server.

Protein modelling

As the PISD protein structure was not available in PDB database, *ab initio* structural modelling was performed. The amino acid sequence (375 aa) of PISD was obtained from UniProtKB (Accession ID: Q9UG56-2). The I-TASSER (Iterative Threading ASSEmbly Refinement) server was used for predicting

protein structure and function. The predicted protein structures for both the wild-type and mutant were evaluated using PyMOL (The PyMOL Molecular Graphics System, Version 1.2r3pre, Schrödinger, LLC). Predicted models were also analyzed using VADAR.

Chemicals, antibodies and reagents

For induction of cellular oxidative stress and/or apoptosis, we used hydrogen peroxide (H_2O_2) (H1009, Sigma-Aldrich), proteasome inhibitor MG-132 (M7449, Sigma-Aldrich), staurosporine (STS) (S5921, Sigma-Aldrich), and recombinant human TNF-α (300-01A, PeproTech) with cycloheximide (CHX) (C4859, Sigma-Aldrich). Ethanolamine (Etn) (E0135, Sigma-Aldrich) was used in the rescue experiment. The following primary antibodies were used for immunoblotting: mouse anti-glycerinaldehyd-3-phosphat-dehydrogenase (GAPDH; ab8245, Abcam), rabbit anti-OPA1 (clone D7C1A, 67589, Cell Signaling Technology), rabbit anti-PISD (HPA031091, Sigma-Aldrich), mouse anti-α-tubulin (clone DM1A, T9026, Sigma), and rabbit anti-VDAC (PA1-954A, Thermo Fisher). Secondary horseradish peroxidase (HRP)-coupled anti-rabbit (NA934V) and anti-mouse (NA931V) antibodies were from GE Healthcare. For immunocytochemistry: mouse anti-cytochrome *c* (Clone 6H2.B4; 12963, Cell Signaling Technology), mouse anti-mitochondria (ab3298, Abcam), Alexa Fluor488 goat anti-mouse (A11001, Life Technologies), and Alexa Fluor546 goat anti-mouse (A11003, Life Technologies).

Cell culture

Primary fibroblasts obtained from a skin biopsy of patient 1 and healthy control individuals were cultured in Dulbecco's modified Eagle medium (DMEM; ThermoFisher) supplemented with 10% fetal bovine serum (FBS; GE Healthcare) and penicillin-streptomycin (100 U/mL and 100 mg/mL, respectively; ThermoFisher) and incubated at 37°C in a humidified atmosphere with 5% CO_2. Cells were tested for mycoplasma contamination and confirmed to be mycoplasma free.

Immunocytochemistry

Fibroblasts were seeded on coverslips and treated with 1 mM H_2O_2 for 1 h, 20 µM MG-132 for 16 h or left untreated under basal, steady-state conditions. Subsequently, cells were rinsed with PBS, fixed with 4% paraformaldehyde (Sigma-Aldrich) in PBS and washed three times with PBS. After treatment with permeabilization/blocking solution (2% BSA, 3% goat serum, 0.5% Nonidet P40 in PBS), cells were incubated in antibody solution (3% goat serum and 0.1% Nonidet P40 in PBS) containing appropriate primary antibodies. Cells were washed with PBS and incubated with Fluorophore-conjugated secondary antibodies in antibody solution. After extensive washing with PBS cells were embedded in ProLong Diamond Antifade Mountant with DAPI (P36962, Life Technologies) on microscopic slides. Cells were analysed using the epifluorescence mode of an Olympus cell tool TIRFM system equipped with a 60x oil immersion objective lens, and pictures of representative cells were taken to visualize changes in mitochondria morphology.

Mitochondria isolation

Mitochondria isolation was performed according to a protocol adapted from (Vogel et al., 2005). Briefly, cells cultured under basal, steady-state conditions were trypsinized, pelleted and washed three times with PBS. Subsequently, cells were resuspended in 500 µL isotonic buffer (0.25 M sucrose, 5 mM Tris-HCl pH 7.5, 1 mM EDTA, supplemented with PhosSTOP and protease inhibitor (Roche)) and broken by 15 strokes through a 0.4 mm needle. Intact cells and cell debris were removed by centrifugation at 600 x g for 15 min at 4°C. Mitochondria were pelleted by subsequent centrifugation of the supernatant at 10,000 x g for 25 min at 4°C. The supernatant containing the cytosolic fraction was removed and diluted in loading buffer (33% glycerol, 80 mM Tris-HCl, pH 6.8, 0.3 M dithiothreitol, 6.7% sodium dodecyl sulphate (SDS), 0.1% bromophenol blue). Mitochondria pellets were resuspended in 2x loading buffer and loaded along with the diluted cytosolic fraction on SDS-PAGE (10%) followed by immunoblotting.

Immunoblotting

Patient- and control-derived fibroblasts were harvested in ice-cold RIPA buffer (50 mM Tris-HCl, pH 8.0; 150 mM NaCl; 1% NP-40; 0.5% sodium deoxycholate; 0.1% SDS supplemented with Mini Protease Inhibitor and PhosSTOP (Roche)) and lysed for 10 min on ice. Cell debris was removed by centrifugation at 20,800 x g for 10 min at 4°C. Protein extracts were diluted in loading buffer, separated on SDS-PAGE under denaturing conditions, and transferred to PVDF membranes (BioRad). Membranes were blocked followed by incubation with the indicated primary antibody overnight at 4°C and by HRP-linked secondary antibodies at room temperature for 1 h. *Chemiluminescent*

western blots were digitally imaged using a ChemiDoc MP (Bio-Rad). Band intensities were determined using the Image Lab v6.0 software (Bio-Rad).

Cell viability

Cells were seeded into 96-well microplates and treated with 1 mM H_2O_2 for 1 h, 1 µM STS for 24 h, 20 µM MG-132 for 16 h, 10 ng/mL TNF-α with 5 µM CHX for 24 h or left untreated under basal, steady-state conditions. For rescue experiments, cells were treated with 1 mM Etn for 22 h, 20 µM MG-132 for 16 h, 1 mM Etn 6 h before and during treatment with 20 µM MG-132 for 16 h, or left untreated. Cell viability was determined with the cell proliferation reagent WST-1 (05015944001, Roche) according to manufacturer's instructions. The tetrazolium salt WST-1 is cleaved to formazan by cellular mitochondrial dehydrogenases. The formazan dye produced by viable cells was quantified by measuring the absorbance at 440 nm by an Epoch microplate spectrophotometer (BioTek Instruments) and the Gen5 v2.09 software (BioTek Instruments).

Caspase activity

Cells were seeded into white flat-bottom 96-well microplates and treated with 1 mM H_2O_2 for 1 h, 1 µM STS for 24 h, 20 µM MG-132 for 16 h, 10 ng/mL TNF-α with 5 µM CHX for 24 h or left untreated under basal, steady-state conditions. For rescue experiments, cells were treated with 1 mM Etn for 22 h, 20 µM MG-132 for 16 h, 1 mM Etn 6 h before and during treatment with 20 µM MG-132 for 16 h or left untreated. To determine caspase-3/7 activity, the Caspase-Glo 3/7 Assay (Promega) was performed according to manufacturer's instructions. Luminescence signals were generated through

the cleavage of the luminogenic caspase-3/7 substrate (containing the caspase-3/7 specific tetrapeptide sequence DEVD) that is further processed by an UltraGlow recombinant luciferase and were measured by the MicroLumat LB96P luminometer (Berthold Technologies) using the WinGlow software v 1.25 (Berthold Technologies).

Data analyses and statistics

Quantitative data are presented as the mean ± standard deviation (SD) performed by GraphPad prism7 software (Instat, GraphPad Software). Statistical significance was assessed by one-way ANOVA for multiple comparison. Statistically significant differences were identified by *post hoc* analysis using Student's *t*-test followed by Bonferroni correction. Assessments were considered significant at *P* value <0.05. *P* value of less than 0.05 was considered statistically significant (*, $P \leq 0.05$; **, $P \leq 0.01$; ***, $P \leq 0.001$; ****, $P \leq 0.0001$).

Results

Clinical and radiographic phenotype

We ascertained two unrelated probands, each originating from an apparently non-consanguineous family. P1 was evaluated for short stature at age 9 months and at age 2 years 11 months. She was born to non-consanguineous parents (Family 1, Figure 1A). Prenatally, at gestational age of 35 weeks, femur length and occipito-frontal circumference (OFC) were noted to be at 2 SD below the mean. She was born at term by cesarean section because of non-progress of labor and weighed 2.5 Kg (-2 SD) at birth. Poor suck, inadequate weight gain, and kyphosis were noted in infancy. Complete

blood counts, liver function tests, respiratory function tests were unremarkable. She had normal serum levels of bicarbonate, 25-hydroxy vitamin D, calcium and phosphorus and urinary levels of calcium and creatinine. Ultrasonogram of abdomen, two-dimensional echocardiography of heart and eye examination were unremarkable at 9 months of age. N-acetylgalactosamine-sulfate sulfatase and beta-galactosidase-1 activity were within normal limits. At age 2 years and 11 months, she had age appropriate intellectual functioning, motor development and social and language skills. Her OFC was 43 cm (-4 SD), length 74 cm (-4 SD) and weight 7.5 Kg (-3.3 SD). Her upper segment to lower segment ratio was 1.31:1. Clinical evaluation revealed a mild facial dysmorphism with a small and pointed chin with retrognathia. The wrists were rather broad and extension in both elbows was limited. Bilateral mild hallux valgus and partial cutaneous syndactyly of toes 2 and 3 were noted in her. Palpation of the abdomen revealed an enlarged liver and spleen. Deep tendon reflexes were unremarkable (Supp. Figure S1). Her vision and hearing were normal. Radiographic examination at age 9 months revealed platyspondyly with anterior beaking of the vertebrae, megaepiphyses with serrated outline of the proximal and distal femora and proximal tibiae, and generalized metaphyseal irregularities of the long bones. However, this had improved by 2 years 11 months of age. The iliac crests were irregular and lace-like, mimicking Dyggve-Melchior-Clausen dysplasia. Middle and proximal phalanges were broad (Figures 2A-G). The skull was unremarkable (Supp. Figure S2).

P2 was assessed at age 9 years for short stature. He was born to non-consanguineous parents (Family 2, Figure 1B). Antenatal course was unremarkable. He was born by cesarean section and weighed 2 Kg at birth. He had normal developmental milestones and had good scholastic performance. His head circumference was 49.5 cm (-3 SD), height 120 cm (-3.3 SD), weight 30 kg (normal) and arm span was 121 cm. Bulbous nose, long philtrum and mild retrognathia were noted. Bilateral mild hallux valgus and mild waddling gait were noted (Supp. Figure S3). He had

unremarkable cardiovascular, respiratory, abdominal and neurological examination. Radiological examination at age of 9 years revealed platyspondyly with wedge shaped vertebrae, mildly large capital femoral epiphyses with coxa vara, and mild metaphyseal dysplasia of the long bones. The epiphyses of the knee were somewhat flat. The short tubular bones were unremarkable (Figures 2H-M). The skull was normal (Supp. Figure S2).

The skeletal phenotypes of the two patients fell into a broad category of SEMD. However, they were unclassifiable, and regarded as different disorders (Supp. Table S2). Trio exome sequencing (proband and parents) in both families did not reveal a mutation in any of the known genes causing a skeletal dysplasia (data not shown). Further search in both patients yielded homozygosity for the same pathogenic variant in the *PISD* gene (see below). The clinical and radiological features were then reviewed (Supp. Table S2). We concluded that both patients showed the age-dependent differences of the same disorder: megaepiphyses and metaphyseal dysplasia became less conspicuous, and coxa vara becomes manifest with advancing of age.

WES identified a homozygous pathogenic *PISD* missense variant in both probands

Exome sequencing data analysis and variant prioritization for both families identified a bi-allelic missense variant, c.797G>A [p.(Cys266Tyr)] in *PISD* (GenBank: NM_178022.1) in the homozygous state (Supp. Figure S4). Sanger analysis confirmed the autosomal recessive segregation of the variant in the both families (Figure 1). This variant is neither present in the gnomAD database nor in the in-house cohort of 362 Indian families (475 exomes, originating from 362 families) with rare Mendelian disorders. Also, multiple *in-silico* prediction tools were consistent in classifying this variant as damaging/disease causing with a CADD score of 32 (Supp. Table S3). The affected amino acid residue

is located in a highly conserved region of PISD (Supp. Figure S5) with GERP++ RS score of 5.73 (Supp. Table S3). The variant details have been submitted to LOVD (https://databases.lovd.nl/shared/genes/PISD).

Homozygosity mapping from the exome data of the probands revealed that the variant is found in the only overlapping homozygous region (3.10 Mb) on chromosome 22 (Supp. Table S4). Further analysis of the region showed that both probands shared the same haplotype in both alleles, suggesting remote inbreeding (Supp. Table S5).

Molecular modeling of wild-type and mutant PISD reveals that Cys266 is involved in hydrogen-bond interaction with Lys262 in wild-type PISD, whereas in the mutant, Tyr266 is predicted to be involved in hydrogen bonds with Asn268 and Thr274. Thus, the substitution Cys266Tyr appeared to result in significant alteration of PISD structure (Supp. Figure S6).

Patient fibroblasts with homozygous *PISD* p.(Cys266Tyr) mutation show mitochondrial fragmentation

PISD codes for the membrane-bound enzyme phosphatidylserine decarboxylase PISD that is localized in the inner mitochondrial membrane. It catalyzes in mammalian cells the decarboxylation of phosphatidylserine (PS) to phosphatidylethanolamine (PE) (Borkenhagen, Kennedy, & Fielding, 1961; Percy, Moore, Carson, & Waechter, 1983). The PISD proenzyme is processed by an autoendoproteolytic cleavage into an α- and β-subunit during import to the inner mitochondrial membrane (IMM), forming an enzymatically active heterodimer that is associated with the IMM (Kuge, Saito, Kojima, Akamatsu, & Nishijima,

1996; Schuiki & Daum, 2009). The PISD substrate PS is produced in the endoplasmatic reticulum (ER) and transported to the mitochondria (Vance & Tasseva, 2013). PE can also be generated via the cytidine diphosphate (CDP)-ethanolamine pathway in the ER (Kennedy & Weiss, 1965). PE is particularly enriched in the IMM, and the PE content is crucial for maintaining normal mitochondrial function (Di Bartolomeo, Doan, Athenstaedt, Becker, & Daum, 2017; Schuiki & Daum, 2009; Vance & Tasseva, 2013). Knock-down of *Pisd* has been shown to impair cell growth and reduce oxidative phosphorylation in CHO cells, and deficiency of *Pisd* in mice results in early embryonic lethality (Steenbergen et al., 2005; Tasseva et al., 2013). We therefore investigated the cellular consequences of the amino acid substitution p.(Cys266Tyr) in PISD in detail and used primary fibroblasts derived from a skin biopsy of patient 1 as cellular model system. The amount of the unprocessed PISD form of 46 kDa was similar in patient 1 and control fibroblasts, indicating that the amino acid change did not affect PISD protein stability (Figure S7). Next, we studied the effect of the *PISD* p.(Cys266Tyr) variant on mitochondrial morphology since *Pisd*$^{-/-}$ mouse embryonic fibroblasts and CHO cells depleted of Pisd show a dramatically altered mitochondrial morphology (Di Bartolomeo et al., 2017; Steenbergen et al., 2005; Tasseva et al., 2013). We cultured fibroblasts under basal, steady-state conditions and stained mitochondria and cytochrome *c*, the latter is localized in the IMM and required for mitochondrial electron transport (Huttemann et al., 2011). The mitochondria in control-derived fibroblasts showed an interconnected dense tubular network around the nucleus with branching tubules into the cellular periphery (Figure 3A and Supp. Figure S8). In patient fibroblasts, the majority of

mitochondria around the nucleus had a small and punctate morphology; in the cellular periphery, tubular mitochondria were observed, similar to control cells (Figure 3A and Supp. Figure S8). These data suggest an increase in mitochondrial fission and fragmentation in patient-derived fibroblasts which is in accordance with previous data studies reporting mitochondrial fragmentation in *Pisd* knock-down cells and *Pisd*$^{-/-}$ mouse fibroblasts (Steenbergen et al., 2005; Tasseva et al., 2013).

The mitochondrial protein optic atrophy 1 (OPA1) is involved in dynamic regulation of the mitochondrial network structure. Eight OPA1 isoforms are expressed in humans, giving rise to a combination of short (s-OPA1) and long (l-OPA1) isoforms. A balance of long and short forms is required to form the mitochondrial network (Anand et al., 2014; Del Dotto, Fogazza, Carelli, Rugolo, & Zanna, 2018; Wai & Langer, 2016). We next determined the amount of short and long OPA1s and the ratio between the s- and l-forms in patient and control fibroblasts. The s-OPA1 to l-OPA1 ratio was 1.0 to 1.2 in control fibroblasts and 1.4 in patient fibroblasts suggesting a slight shift toward more s-OPA1 in patient cells, however, this was not statistically significant (Figures 3B and C). The finding of mitochondria network fragmentation in patient fibroblasts is suggestive of an impaired mitochondrial function, possibly leading to an increased sensitivity to oxidative stress.

Mitochondrial stressors induce a decrease in cell viability and an increase in caspase-3/7 activity in patient-derived fibroblasts

Fragmentation of the mitochondrial network is linked to mitochondrial dysfunction, and fragmented mitochondria, during oxidative stress, can trigger the intrinsic pathway of apoptosis (Jezek, Cooper, & Strich, 2018). To determine the effects of oxidative stress induced by external stimuli, we treated patient and control fibroblast cells with H_2O_2 or the proteasome inhibitor MG-132 that both enhance intracellular production of reactive oxygen species (ROS) (Rigoulet, Yoboue, & Devin, 2011; Wu, Chi, & Lin, 2002). When H_2O_2 and MG-132 were applied, both control- and patient-derived fibroblasts showed a perinuclear compaction of mitochondria. Their tubular structure was impaired, and mitochondrial tubules in the cellular periphery were reduced or absent (Supp. Figure S9). In a next step, we examined the effect of H_2O_2 on cell viability and apoptosis. Pro-apoptotic proteins that are activated by this cellular stress stimulate the intrinsic apoptosis pathway via mitochondrial permeabilization and cytochrome *c* release that in turn activate the effector caspases-3 and -7 which execute cell death (Cory & Adams, 2002; Elmore, 2007). Treatment of fibroblasts with H_2O_2 caused a drastically reduced cell viability in control cells down to 54-61% compared to the viability of untreated cells (set to 100%) (Supp. Figure S10). Similarly, patient fibroblasts showed a decrease down to ~46% that was not significantly different to control cells (Supp. Figure S10). When we determined the activity of caspase-3 and -7, we did not detect any activation of the two caspases in patient and control fibroblasts after H_2O_2 treatment (Supp. Figure S10). H_2O_2 seemed to impair cell growth in control and patient

fibroblasts to the same extent, however, we did not observe any activation of caspase-3 and -7 in the cells under this condition. To detect possible differences in cell viability and activation of the intrinsic apoptosis pathway between control and patient cells, we stressed fibroblasts with MG-132 or staurosporine (STS). MG-132 induces activation of the intrinsic apoptosis pathway leading to activation of caspase-3 (Almond et al., 2001; Han et al., 2010; Qui et al., 2000), similar to STS that stimulates apoptosis via caspase-9 and caspase-3 activation (Caballero-Benitez & Moran, 2003; Tafani, Minchenko, Serroni, & Farber, 2001). In control fibroblasts, cell viability was decreased by 15-18% and 18-27% after treatment with MG-132 and STS, respectively (Figures 4A and B). In contrast, patient fibroblasts showed a decrease in cell viability down to ~59% and ~54% for MG-132 and STS compared to untreated cells, respectively, indicating a significantly reduced viability in patient compared to control fibroblasts under these conditions (Figures 4A and B). In addition, incubation with MG-132 enhanced the activity of caspase-3 and -7 in patient-derived cells by 5.7-fold in comparison to untreated cells, whereas the activity of both enzymes was similar in MG-132-treated and untreated control fibroblasts (Figure 4C). A similar effect was identified after STS treatment. This drug significantly increased the activity of caspase-3 and -7 by 7.4-fold in patient cells, whereas a 2.4- to 4.1-fold increase was detected in control cells (Figure 4D). Finally, we incubated control and patient cells with TNF-α and cycloheximide (CHX) to analyze the effect of these drugs on the extrinsic pathway of apoptosis (Gupta, 2002). Although we identified a significantly reduced cell viability in patient compared to control 1 cells, we did not observe any statistically significant

difference in caspase-3 and -7 activation between the three control and patient fibroblasts (Supp. Figure S11). Together, our data demonstrate an enhanced susceptibility of patient-derived fibroblasts to oxidative stress, induced by MG-132 and STS that resulted in reduced cell viability and increased cell death, likely via the intrinsic apoptosis pathway.

Ethanolamine supplementation largely restores cell viability and reduces activity of apoptotic proteases in MG-132-stressed patient cells

Based on our data that fibroblasts with the homozygous *PISD* mutation p.(Cys266Tyr) show fragmented mitochondria and decreased cell viability, we assumed that the PE content in the IMM may be reduced leading to disruption of the *mitochondrial membrane integrity*. As mentioned above, PE can be generated by PISD, but also by the CDP-ethanolamine pathway (Kennedy & Weiss, 1965; Vance & Tasseva, 2013). Previous studies showed that exogenous ethanolamine (Etn) can be processed by the CDP-ethanolamine pathway and increase the cellular PE amount, for example in a yeast mutant with phosphatidylserine decarboxylase deletion (Rockenfeller et al., 2015; S. Wang et al., 2014). We therefore examined if Etn supplementation could rescue reduced *cell viability* and increased apoptosis following MG-132 treatment in patient cells. Treatment of control and patient cells with Etn alone had no effect on cell viability and activity of caspase-3 and -7 (Figures 5A and B). As observed before, MG-132 treatment induced a drastic decrease in cell viability down to 59% in patient cells (compare Figure 5A and 4A), while Etn supplementation of MG-132-treated patient cells significantly improved cell viability as it was reduced to only 72% compared to

untreated cells (Figure 5A). A similar but more drastic effect was observed for caspase-3 and -7 activity: patient cells treated with MG-132 and supplemented with Etn showed a statistically reduced activation of both apoptotic proteases in comparison to patient cells treated with MG-132 alone (2.8-fold for Etn + MG-132 versus 5.7-fold for MG-132; Figure 5B). Together, these data demonstrate that Etn administration significantly rescued cell viability and caspase-3/7 activation in patient cells with the *PISD* variant p.(Cys266Tyr). This finding is line with previous data showing that mitochondrial defects can be reversed when the mitochondrial PE content is increased by PE supplementation in CHO cells with a chronically reduced synthesis of mitochondrial PE (Tasseva et al., 2013).

Discussion

We report on two children with a novel spondyloepimetaphyseal dysplasia with severe platyspondyly, generalized metaphyseal dysplasia with lace ilia, and megaepiphyses at younger age. However, metaphyseal dysplasia and megaepiphysis became less conspicuous with advancing of age. The skeletal phenotype in late childhood was not so distinctive. The early manifestation, apart from magaepiphyses, somewhat resembles that of Dyggve-Melchior-Clausen dysplasia (MIM# 223800) because of lace ilia. The late manifestation may be descriptively termed SMD A4 rather than SEMD because of regressive epiphyseal changes with age (MIM# 609052). Trio exome sequencing identified a homozygous missense variant c.797G>A; p.(Cys266Tyr) in the *PISD* gene in both affected individuals. Exome data and ROH analysis revealed that both patients shared a common haplotype around the *PISD* gene, indicating a remote relationship.

PISD encodes mitochondrial phosphatidylserine decarboxylase that catalyzes decarboxylation of phosphatidylserine to phosphatidylethanolamine. PISD is essential for development as deletion of *Pisd* is lethal in mice indicating that mammalian development depends on sufficient supply of PE (Steenbergen et al., 2005). We postulate that the substitution of cysteine 266 by tyrosine in *PISD* represents a hypomorphic allele which reduces enzymatic activity in patient cells. While this manuscript was under review, Shutt and colleagues reported biallelic *PISD* variants in two sisters with short stature, platyspondyly, metaphyseal striations, craniofacial dysmorphism, congenital cataracts, and bilateral hearing loss (https://www.biorxiv.org/content/early/2018/09/12/413070) that confirmed our findings. Both affected females carried the intronic c.595+5G>A change and the c.728G>A variant predicting the amino acid change p.(Arg243Gln) (according to the canonical transcript NM_178022.1). The c.595+5G>A change caused the production of an alternatively spliced product, however, the exact effect on mRNA level, such as *in-frame* deletion or introduction of a premature stop codon has not been determined. The p.(Arg243Gln) change was shown to impair PISD activity by reducing autocatalytic proteolysis and thereby the generation of the 12 kDa α and the 30 kDa β PISD subunits (https://www.biorxiv.org/content/early/2018/09/12/413070). These data together with our findings provide evidence for decreased, but not completely abolished PISD activity in the four patients, ultimately resulting in reduced amount of mitochondrial PE and impaired mitochondrial homeostasis.

Moderate depletion of mitochondrial PE has been shown to impair cell growth and alter mitochondrial morphology and function in CHO cells (Tasseva et al., 2013). In line with these findings, we identified small and fragmented mitochondria in patient-derived fibroblasts cultured under basal conditions. Fragmentation of the mitochondrial network has been linked to enhanced ROS formation, and oxidative stress can further stimulate the intrinsic pathway of apoptosis (Jezek

et al., 2018). Indeed, we demonstrated that fibroblasts with the *PISD* mutation p.(Cys266Tyr) show decreased cell viability and increased stimulation of the proapoptotic enzymes caspase-3 and -7 when treated with STS or MG-132. The data suggest enhanced susceptibility of patient cells to oxidative stress triggering cell death, most likely via the intrinsic apoptotic pathway as shown here by treatment of the cells with MG-132, STS and TNF-α together with CHX. Remarkably, Etn supplementation to MG-132-stressed *PISD* mutation-positive fibroblasts largely restored cell viability and drastically decreased activation of the effector caspases 3 and 7. These data provide evidence for a reduced content of PE in patient cells and that PE administration may restore mitochondrial PE content and thereby mitochondrial function. A general positive effect of Etn on mammalian cells has recently been demonstrated. Etn addition to U2OS and H4 cell cultures leads to increased cellular PE levels, induces autophagy, and reduces chronological senescence (Rockenfeller et al., 2015). Together with our data from rescue experiments, these findings suggest that PE may constitute a limiting factor for autophagy in particular and cell survival and longevity in general (Rockenfeller et al., 2015). In line with this, the importance of PISD-derived mitochondrial PE for autophagy has recently been demonstrated (Thomas et al., 2018).

The novel form of SEMD that we presented is a new comer in a group of skeletal dysplasias related to impairment of mitochondrial proteins. This group comprises only a few skeletal disorders, including X-linked SEMD (MIM# 313400), CODAS syndrome (MIM# 600373), EVEN-PLUS syndrome (MIM# 616854), and MAGMAS dysplasia (MIM# 613320). The missense variant p.(Asp237Gly) in the X-linked *AIFM1* gene, encoding apoptosis inducing factor mitochondria associated 1 protein, has been identified in two families from Poland with several boys affected by X-linked SEMD with progressive neurodegeneration (Mierzewska et al., 2017). The multi-system developmental disorder CODAS (cerebral, ocular, dental, auricular, skeletal) syndrome is caused by bi-allelic mutations in

LONP1 (Strauss et al., 2015). *LONP1* encodes Lon protease that is required for assembly of respiratory-chain complexes within the IMM and maintenance of mitochondrial homeostasis beside other cellular functions (Pinti et al., 2016). Mutations in *HSPA9* have been detected in the autosomal recessively inherited EVEN-PLUS syndrome (for epiphyseal, vertebral, ear, nose, plus associated findings) (Royer-Bertrand et al., 2015). HSPA9 is a mitochondrial chaperone that participates in the import of proteins to the mitochondrial matrix, their folding and degradation (Flachbartova & Kovacech, 2013). In another new form of skeletal dysplasias, bi-allelic mutations have been identified in the mitochondria-associated granulocyte macrophage colony stimulating factor-signaling gene (*MAGMAS*) (Mehawej et al., 2014). Most of the clinical manifestations observed in the aforementioned disorders are atypical for classical mitochondrial diseases (Royer-Bertrand et al., 2015; Strauss et al., 2015).

It still remains unclear how precisely defects in mitochondrial components and enzymes can cause a generalized skeletal disorder. Several possible scenarios can be envisioned: (i) the mutated mitochondrial proteins have a role in embryonic (skeletal) development (Royer-Bertrand et al., 2015), (ii) patient cells have only limited capacity to increase ATP production during increased cellular stress (Strauss et al., 2015), (iii) mutant cells show diminished cell proliferation and/or enhanced induction of cell death, possibly triggered by oxidative stress (this work and Glazov et al., 2011; Mehawej et al., 2014). In line with the latter hypothesis, a recent paper reported *GPX4* mutations in the Sedaghatian-type spondylometaphyseal dysplasia (SMDS; MIM# 250220) (Smith et al., 2014). GPX4 is a member of the glutathione peroxidase family protecting the organism from oxidative damage (Brigelius-Flohe & Maiorino, 2013). Similar to *Pisd* knockout mice, *Gpx4*-deficient mice die during early embryonic development, and loss of Gpx4 has been shown to trigger apoptosis in neural cells (Imai et al., 2003; Seiler et al., 2008; Yant et al., 2003). Further

investigations are needed to delineate the mechanistic defects in mitochondrial function associated with SEMD, SMDS and other skeletal dysplasias. However, consumption of ethanolamine-rich food may positively influence the clinical course of patients with biallelic *PISD* mutations.

Acknowledgements

We thank the patients and their families for the participation in this study and the Microscopy Imaging Facility at the University Medical Center Hamburg-Eppendorf (UMIF) for technical support.

Supplemental Data

Supplemental Data include eleven figures and five tables.

Competing interests

The authors declare no competing interests.

REFERENCES

Almond, J. B., Snowden, R. T., Hunter, A., Dinsdale, D., Cain, K., & Cohen, G. M. (2001). Proteasome inhibitor-induced apoptosis of B-chronic lymphocytic leukaemia cells

involves cytochrome c release and caspase activation, accompanied by formation of an 700 kDa Apaf-1 containing apoptosome complex. *Leukemia, 15*(9), 1388–1397.

Anand, R., Wai, T., Baker, M. J., Kladt, N., Schauss, A. C., Rugarli, E., & Langer, T. (2014). The i-AAA protease YME1L and OMA1 cleave OPA1 to balance mitochondrial fusion and fission. *The Journal of Cell Biology, 204*(6), 919–929.

Bonafe, L., Cormier-Daire, V., Hall, C., Lachman, R., Mortier, G., Mundlos, S., . . . Unger, S. (2015). Nosology and classification of genetic skeletal disorders: 2015 revision. *American Journal of Medical Genetics Part A, 167A*(12), 2869–2892.

Borkenhagen, L. F., Kennedy, E. P., & Fielding, L. . (1961). Enzymatic Formation and Decarboxylation of Phosphatidylserine. *Journal of Biological Chemistry, 236*, PC28-PC30.

Brigelius-Flohe, R., & Maiorino, M. (2013). Glutathione peroxidases. *Biochimica et Biophysica Acta, 1830*(5), 3289–3303.

Caballero-Benitez, A., & Moran, J. (2003). Caspase Activation Pathways Induced by Staurosporine and Low Potassium: Role of Caspase-2. *Journal of Neuroscience Research, 71*(3), 383–396.

Cory, S., & Adams, J. M. (2002). The Bcl2 family: regulators of the cellular life-or-death switch. *Nature Reviews Cancer, 2*(9), 647–656.

Del Dotto, V., Fogazza, M., Carelli, V., Rugolo, M., & Zanna, C. (2018). Eight human OPA1 isoforms, long and short: What are they for? *Biochimica et Biophysica Acta, 1859*(4), 263–269.

Di Bartolomeo, F., Doan, K. N., Athenstaedt, K., Becker, T., & Daum, G. (2017). Involvement of a putative substrate binding site in the biogenesis and assembly of phosphatidylserine decarboxylase 1 from Saccharomyces cerevisiae. *Biochimica et Biophysica Acta, 1862*(7), 716–725.

Elmore, S. (2007). Apoptosis: A Review of Programmed Cell Death. *Toxicologic Pathology, 35*(4), 495–516.

Flachbartova, Z., & Kovacech, B. (2013). Mortalin - a multipotent chaperone regulating cellular processes ranging from viral infection to neurodegeneration. *Acta Virologica, 57*(1), 3–15.

Glazov, E. A., Zankl, A., Donskoi, M., Kenna, T. J., Thomas, G. P., Clark, G. R., . . . Brown, M. A. (2011). Whole-exome re-sequencing in a family quartet identifies POP1 mutations as the cause of a novel skeletal dysplasia. *PLoS Genetics, 7*(3), e1002027.

Guernsey, D. L., Jiang, H., Evans, S. C., Ferguson, M., Matsuoka, M., Nightingale, M., . . . Samuels, M. E. (2009). Mutation in pyrroline-5-carboxylate reductase 1 gene in families with cutis laxa type 2. *The American Journal of Human Genetics, 85*(1), 120–129.

Gupta, S. (2002). A decision between life and death during TNF-alpha-induced signaling. *Journal of Clinical Immunology, 22*(4), 185–194.

Han, Y. H., Moon, H. J, You, B. R., Yang, Y. M., Kim, S. Z., Kim, S. H., & H., Park. W. (2010). MG132, A Proteasome Inhibitor, Induced Death of Calf Pulmonary Artery Endothelial Cells via Caspase-dependent Apoptosis and GSH Depletion. *Anticancer Research, 30*(3), 879–886.

Huttemann, M., Pecina, P., Rainbolt, M., Sanderson, T. H., Kagan, V. E., Samavati, L., . . . Lee, I. (2011). The multiple functions of cytochrome c and their regulation in life and death decisions of the mammalian cell: From respiration to apoptosis. *Mitochondrion, 11*(3), 369–381.

Imai, H., Hirao, F., Sakamoto, T., Sekine, K., Mizukura, Y., Saito, M., . . . Nakagawa, Y. (2003). Early embryonic lethality caused by targeted disruption of the mouse PHGPx gene. *Biochemical and Biophysical Research Communications, 305*(2), 278–286.

Jezek, J., Cooper, K. F., & Strich, R. (2018). Reactive Oxygen Species and Mitochondrial Dynamics: The Yin and Yang of Mitochondrial Dysfunction and Cancer Progression. *Antioxidants (Basel), 7*(1), pii: E13.

Kancheva, D., Atkinson, D., De Rijk, P., Zimon, M., Chamova, T., Mitev, V., . . . Jordanova, A. (2016). Novel mutations in genes causing hereditary spastic paraplegia and Charcot-Marie-Tooth neuropathy identified by an optimized protocol for homozygosity mapping based on whole-exome sequencing. *Genetics in Medicine, 18*(6), 600–607

Kennedy, E. P. , & Weiss, S. B. (1965). The function of cytidine coenzymes in the biosynthesis of phospholipids. *Journal of Biological Chemistry, 222*, 193–214.

Kuge, O., Saito, K., Kojima, M., Akamatsu, Y., & Nishijima, M. (1996). Post-translational processing of the phosphatidylserine decarboxylase gene product in Chinese hamster ovary cells. *Biochemical Journal, 319 (Pt 1)*, 33–38.

Li, H., & Durbin, R. (2009). Fast and accurate short read alignment with Burrows-Wheeler transform. *Bioinformatics, 25*(14), 1754–1760.

McKenna, A., Hanna, M., Banks, E., Sivachenko, A., Cibulskis, K., Kernytsky, A., . . . DePristo, M. A. (2010). The Genome Analysis Toolkit: a MapReduce framework for analyzing next-generation DNA sequencing data. *Genome Research, 20*(9), 1297–1303.

Mehawej, C., Delahodde, A., Legeai-Mallet, L., Delague, V., Kaci, N., Desvignes, J. P., . . . Megarbane, A. (2014). The impairment of MAGMAS function in human is responsible for a severe skeletal dysplasia. *PLoS Genetics, 10*(5), e1004311.

Mierzewska, H., Rydzanicz, M., Bieganski, T., Kosinska, J., Mierzewska-Schmidt, M., Lugowska, A., . . . Ploski, R. (2017). Spondyloepimetaphyseal dysplasia with neurodegeneration associated with AIFM1 mutation - a novel phenotype of the mitochondrial disease. *Clinical Genetics, 91*(1), 30–37.

Ng, S. B., Buckingham, K. J., Lee, C., Bigham, A. W., Tabor, H. K., Dent, K. M., . . . Bamshad, M. J. (2010). Exome sequencing identifies the cause of a mendelian disorder. *Nature Genetics, 42*(1), 30–35.

Pansuriya, T. C., van Eijk, R., d'Adamo, P., van Ruler, M. A., Kuijjer, M. L., Oosting, J., . . . Bovee, J. V. (2011). Somatic mosaic IDH1 and IDH2 mutations are associated with enchondroma and spindle cell hemangioma in Ollier disease and Maffucci syndrome. *Nature Genetics, 43*(12), 1256–1261.

Percy, A. K., Moore, J. F., Carson, M. A., & Waechter, C. J. (1983). Characterization of brain phosphatidylserine decarboxylase: localization in the mitochondrial inner membrane. *Archives of Biochemistry and Biophysics, 223*(2), 484–494.

Pinti, M., Gibellini, L., Nasi, M., De Biasi, S., Bortolotti, C. A., Iannone, A., & Cossarizza, A. (2016). Emerging role of Lon protease as a master regulator of mitochondrial functions. *Biochimica et Biophysica Acta, 1857*(8), 1300–1306.

Qui, J. H., Asai, A., Chi, S., Saito, N., Hamada, H., & Kirino, T. (2000). Proteasome Inhibitors Induce Cytochrome c–Caspase-3-Like Protease-Mediated Apoptosis in Cultured Cortical Neurons. *The Journal of Neuroscience, 20*(1), 259–265.

Rigoulet, M., Yoboue, E. D., & Devin, A. (2011). Mitochondrial ROS generation and its regulation: mechanisms involved in H(2)O(2) signaling. *Antioxidants & Redox Signaling, 14*(3), 459–468.

Rockenfeller, P., Koska, M., Pietrocola, F., Minois, N., Knittelfelder, O., Sica, V., . . . Madeo, F. (2015). Phosphatidylethanolamine positively regulates autophagy and longevity. *Cell Death & Differentiation, 22(*3), 499–508.

Royer-Bertrand, B., Castillo-Taucher, S., Moreno-Salinas, R., Cho, T. J., Chae, J. H., Choi, M., . . . Superti-Furga, A. (2015). Mutations in the heat-shock protein A9 (HSPA9) gene cause the EVEN-PLUS syndrome of congenital malformations and skeletal dysplasia. *Scientific Reports, 5*, 17154.

Schuiki, I., & Daum, G. (2009). Phosphatidylserine decarboxylases, key enzymes of lipid metabolism. *IUBMB Life, 61*(2), 151–162.

Seiler, A., Schneider, M., Forster, H., Roth, S., Wirth, E. K., Culmsee, C., . . . Conrad, M. (2008). Glutathione peroxidase 4 senses and translates oxidative stress into 12/15-lipoxygenase dependent- and AIF-mediated cell death. *Cell Metabolism, 8*(3), 237–248.

Smith, A. C., Mears, A. J., Bunker, R., Ahmed, A., MacKenzie, M., Schwartzentruber, J. A., . . . Graham, G. E. (2014). Mutations in the enzyme glutathione peroxidase 4 cause Sedaghatian-type spondylometaphyseal dysplasia. *Journal of Medical Genetics, 51*(7), 470–474.

Steenbergen, R., Nanowski, T. S., Beigneux, A., Kulinski, A., Young, S. G., & Vance, J. E. (2005). Disruption of the phosphatidylserine decarboxylase gene in mice causes embryonic lethality and mitochondrial defects. *Journal of Biological Chemistry, 280*(48), 40032–40040.

Strauss, K. A., Jinks, R. N., Puffenberger, E. G., Venkatesh, S., Singh, K., Cheng, I., . . . Suzuki, C. K. (2015). CODAS syndrome is associated with mutations of LONP1, encoding mitochondrial AAA+ Lon protease. *The American Journal of Human Genetics, 96*(1), 121–135.

Tafani, M., Minchenko, D. A., Serroni, A., & Farber, J. L. (2001). Induction of the Mitochondrial Permeability Transition Mediates the Killing of HeLa Cells by Staurosporine. *Cancer Research, 61*(6), 2459–2466.

Tasseva, G., Bai, H. D., Davidescu, M., Haromy, A., Michelakis, E., & Vance, J. E. (2013). Phosphatidylethanolamine deficiency in Mammalian mitochondria impairs oxidative phosphorylation and alters mitochondrial morphology. *Journal of Biological Chemistry, 288*(6), 4158–4173.

Thomas, H. E., Zhang, Y., Stefely, J. A., Veiga, S. R., Thomas, G., Kozma, S. C., & Mercer, C. A. (2018). Mitochondrial Complex I Activity Is Required for Maximal Autophagy. *Cell Reports, 24*(9), 2404–2417.

Vance, J. E., & Tasseva, G. (2013). Formation and function of phosphatidylserine and phosphatidylethanolamine in mammalian cells. *Biochimica et Biophysica Acta, 1831*(3), 543–554.

Vogel, R. O., Janssen, R. J., Ugalde, C., Grovenstein, M., Huijbens, R. J., Visch, H. J., . . . Nijtmans, L. G. (2005). Human mitochondrial complex I assembly is mediated by NDUFAF1. *The FEBS Journal, 272*(20), 5317–5326.

Wai, T., & Langer, T. (2016). Mitochondrial Dynamics and Metabolic Regulation. *Trends in Endocrinology & Metabolism, 27*(2), 105–117.

Wang, K., Li, M., & Hakonarson, H. (2010). ANNOVAR: functional annotation of genetic variants from high-throughput sequencing data. *Nucleic Acids Research, 38*(16), e164.

Wang, S., Zhang, S., Liou, L. C., Ren, Q., Zhang, Z., Caldwell, G. A., . . . Witt, S. N. (2014). Phosphatidylethanolamine deficiency disrupts α-synuclein homeostasis in yeast and worm models of Parkinson disease. *Proceedings of the National Academy of Sciences of the United States of America, 1111*(38), E3976–E3985.

Wu, H.M., Chi, K.H., & Lin, W.W. (2002). Proteasome inhibitors stimulate activator protein-1 pathway via reactive oxygen species production. *FEBS Letters, 526*(1-3), 101–105.

Yang, H., & Wang, K. (2015). Genomic variant annotation and prioritization with ANNOVAR and wANNOVAR. *Nature Protocols, 10*(10), 1556–1566.

Yant, L. J., Ran, Q., Rao, L., Van Remmen, H., Shibatani, T., Belter, J. G., . . . Prolla, T. A. (2003). The selenoprotein GPX4 is essential for mouse development and protects from radiation and oxidative damage insults. *Free Radical Biology and Medicine, 34*(4), 496–502.

Figure titles and legends:

Figure 1 Pedigrees and segregation of the *PISD* variant

(A) Pedigree of family 1 showing segregation of the *PISD* variant c.797G>A (NM_178022.1) as identified by Sanger-sequencing. **(B)** Pedigree of family 2 showing segregation of the *PISD* variant c.797G>A as identified by Sanger-sequencing. Probands (P) are indicated by an arrow.

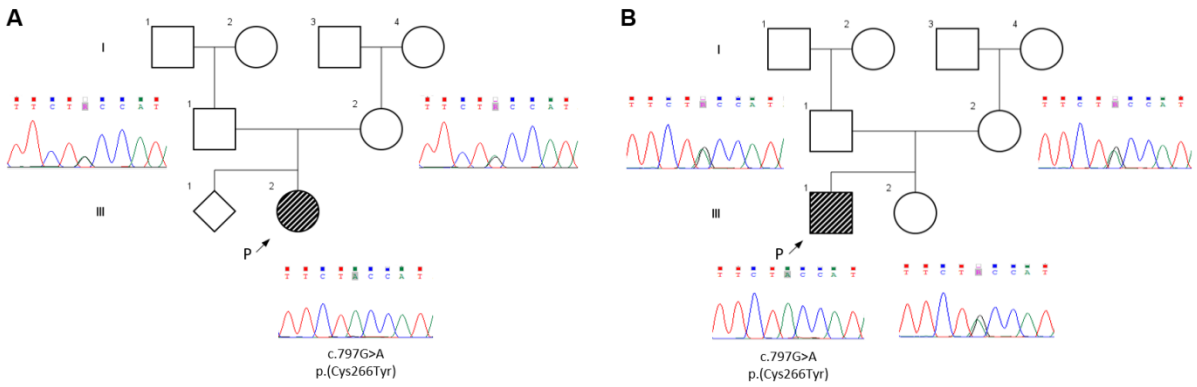

Figure 2 Skeletal survey of the two probands

(A-G) Skeletal survey of the proband P1 at the age of 9 months (A-C) and at 2 years and 11 months (D-G). Metaphyseal cupping is visible at both the proximal and distal ends of the ribs (A, B, D). The spine shows platyspondyly with anteriorly pointed vertebrae (B, E). Early on, at the age of 9 months, the lumbar vertebrae have an ovoid shape (B). The pelvis at 9 months (C) shows irregular iliac crests which normalized at the age of 2 years and 11 months (F). The proximal femoral epiphyses are large and ballooned and flanked by an irregular and spiky metaphysis and short femoral neck (F). The knees are abnormal with large epiphyses and irregular, partly sclerotic distal femoral metaphyses (C). The proximal and middle phalanges are relatively broad in comparison with the rather slender metacarpals (G). Mild metaphyseal changes are also present in the wrists. **(H-M)** Skeletal survey of proband P2 at the age of 9 years. The spine reveals platyspondyly with wedge-shaped vertebrae (H). The metacarpals and phalanges in the hands are unremarkable (J). The feet show bilateral hallux valgus (K). The pelvis is abnormal with coxa vara, large femoral epiphyses and short femoral necks (L). Mild metaphyseal changes are present in the knees (M).

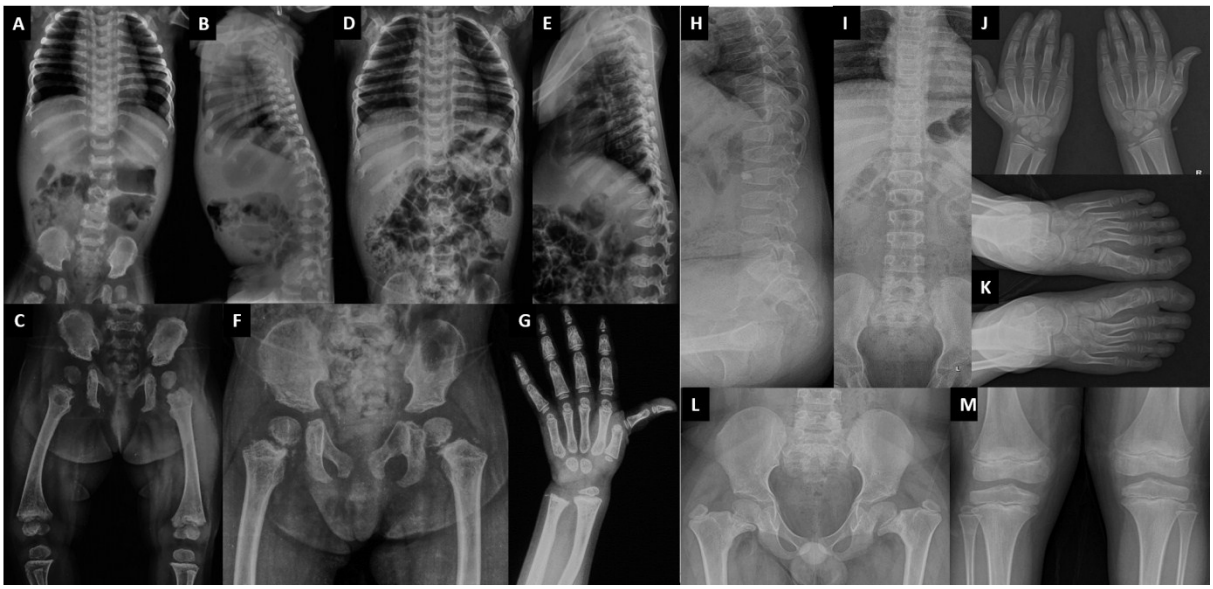

Figure 3 Patient-derived fibroblasts cultured under basal, steady-state conditions show fragmented mitochondria morphology

(A) Fibroblasts were seeded on glass slides, cultured under basal, steady state-conditions, fixed, permeabilized and blocked. Mitochondria were stained by anti-cytochrome *c* antibody followed by anti-mouse Alexa Fluor488-conjugated antibody, and nuclear DNA was labeled by DAPI. Cells were imaged by epifluorescence microscopy. Scale bars, 10 µm. White arrows point to fragmented rounded mitochondria in patient-derived fibroblasts. **(B)** Cell lysates obtained from patient and control fibroblast cultures were fractionated as described in material and methods. Cytosolic and mitochondrial fractions were subjected to SDS-PAGE followed by immunoblotting. The amount of small (80 kDa; s-OPA1) and large (100 kDa; l-OPA1) isoforms of OPA1 was monitored by using an anti-OPA1 antibody. Enrichment of the mitochondrial fraction was verified by an antibody against the mitochondrial membrane protein VDAC. Anti-α-tubulin and anti-GAPDH antibody were used to control for equal loading. **(C)** Band intensities of chemiluminescence reaction were quantified. The mean of four (except Ctrl 2: n=3) independent experiments ± SD is given. One-way ANOVA between groups: $P < 0.01$. *Post hoc P* values were calculated by *t*-tests and Bonferroni correction; ns, not significant. Ctrl 1, 2 and 4, control fibroblasts.

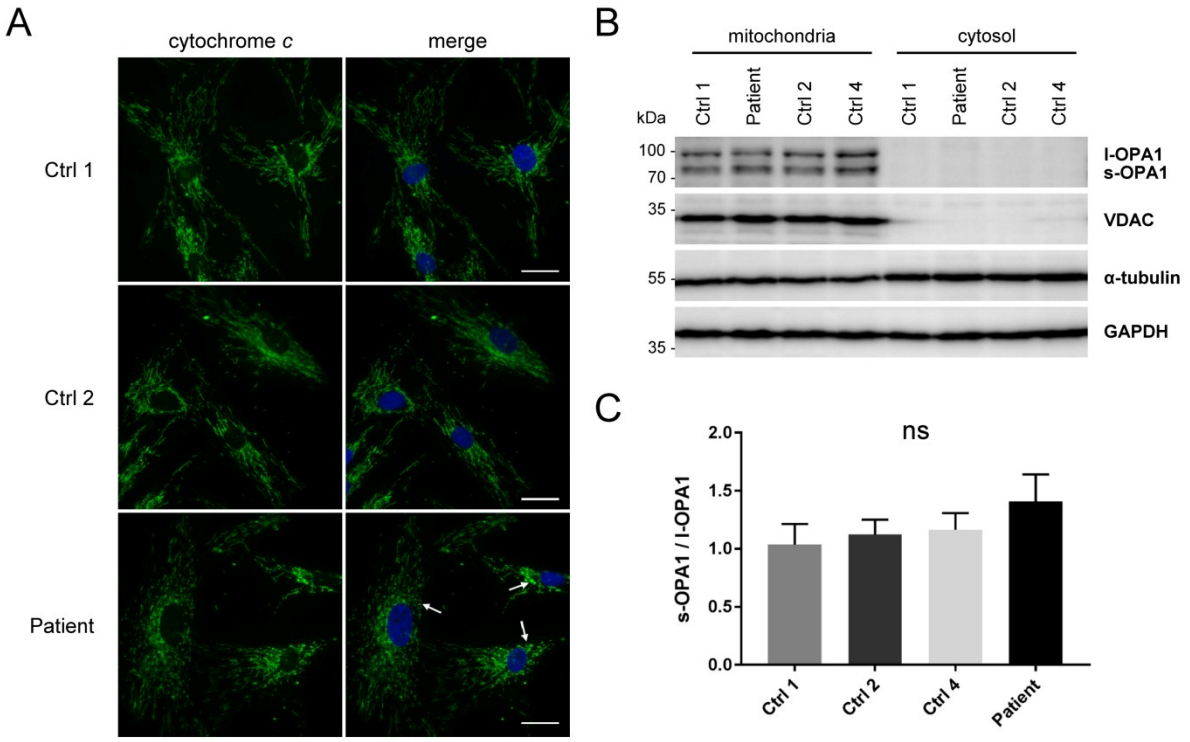

Figure 4 Mitochondrial stressors induce a decrease in cell viability and an increase in caspase-3/7 activation in patient-derived fibroblasts

Fibroblasts were seeded into 96-well microplates and treated with 20 µM MG-132 for 16 h, 1 µM staurosporine (STS) for 24 h or left untreated. **(A, B)** Cell viability was determined by incubation of cells with WST-1 reagent for 30 min and measuring absorbance at 440 nm. **(C, D)** Caspase-3/7 activity was determined by Caspase-Glo 3/7 Assay. Luminescence signals were detected as relative light units by luminometer. The mean ratio of treated to untreated (set as 100%) cells of three (B, D), five (C, except Patient: n=4) and six (A) independent experiments ± SD is given. One-way ANOVA between groups: $P < 0.01$ (B), $P < 0.0001$ (A, C, D). *Post hoc P* values were calculated by *t*-tests and Bonferroni correction; *, $P \leq 0.05$; **, $P \leq 0.01$; ***, $P \leq 0.001$. Ctrl 1-4, control fibroblasts.

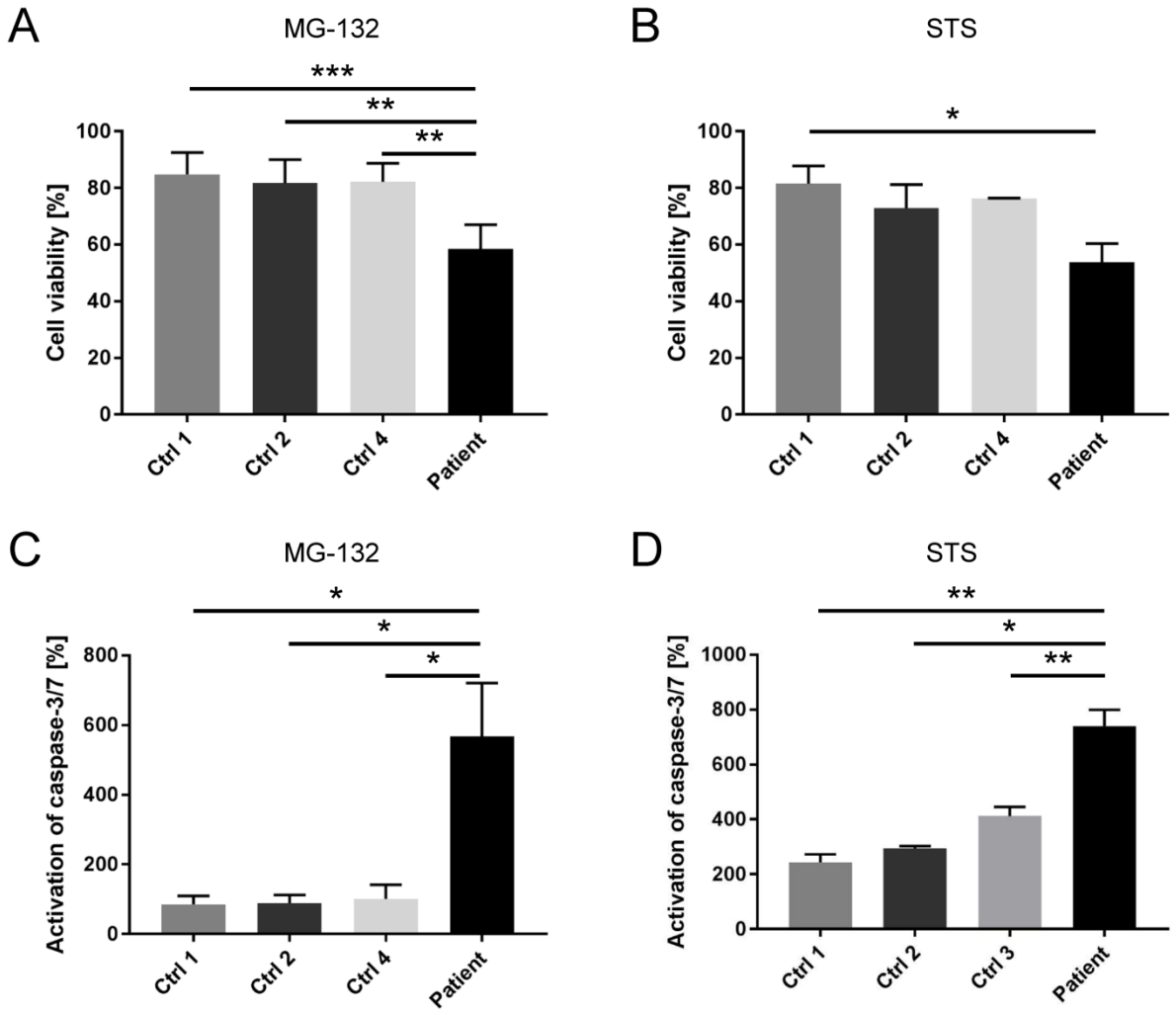

Figure 5 Ethanolamine supplementation rescues MG-132-induced decrease in cell viability and increase in caspase-3/7 activation in patient-derived fibroblasts

Fibroblasts were seeded into 96-well microplates and treated with 1 mM ethanolamine (Etn) for 22 h, 20 µM MG-132 for 16 h, 1 mM Etn 6 h before and during treatment with 20 µM MG-132 for 16 h or left untreated. **(A)** Cell viability was determined by incubation of cells with WST-1 reagent for 30 min and measuring absorbance at 440 nm. **(B)** Caspase-3/7 activity was determined by Caspase-Glo 3/7 Assay. Luminescence signals were detected as relative light units by luminometer. The mean ratio of treated to untreated (set as 100%) cells of three (B, 1 mM Etn; 1 mM Etn + 20 µM MG-132), four (A, 1 mM Etn; 1 mM Etn + 20 µM MG132, except Ctrl 1: n=3), five (B, 20 µM MG-132, except Patient: n=4) and six (A, 20 µM MG-132) independent experiments ± SD is given. One-way ANOVA between groups: $P < 0.05$ (A), $P < 0.001$ (B). *Post hoc P* values were calculated by *t*-tests and Bonferroni correction; *, $P \leq 0.05$. Ctrl 1, 2 and 4, control fibroblasts.